BMC Cancer

RESEARCH

Open Access

Limonoid-rich fraction from *Azadirachta indica* A. Juss. (neem) stem bark triggers ROS-independent ER stress and induces apoptosis in 2D cultured cervical cancer cells and 3D cervical tumor spheroids

Saurav Kumar[1], Bishnu Das[2], Garima Maurya[1], Shreya Dey[1], Parna Gupta[2] and Jayasri Das Sarma[1*]

Abstract

Background The existing anticancer drugs in clinical practice show poor efficacy in cervical cancer patients and are associated with multiple side effects. Our previous study demonstrated the strong antineoplastic activity of crude extract prepared from the stem bark of *Azadirachta indica* (Neem) against cervical cancer. However, the active phytoconstituents of neem stem bark extract and its underlying anticancer mechanism are yet to be investigated. Thus, the present study aimed to identify the active fraction from crude neem stem bark extract to further dissect its anticancer mechanism and determine the active components.

Methods Dichloromethane (DCM) extract from neem stem bark was prepared and fractionated using thin-layer chromatography. The fractions obtained were screened against HeLa and ME-180 cervical cancer cell lines to identify the most active fraction, which was then selected for further studies. Clonogenic assay, cell cycle analysis, apoptosis assay, and reactive oxygen species (ROS) assay were performed to determine the cytotoxicity of the active fraction. Gene expression was analyzed using real-time PCR and western blot to determine the mechanism. Additionally, the HeLa cells-derived 3D spheroid model was used to determine the antitumor efficacy of the active fraction. Electrospray ionization-mass spectrometry, Fourier-transform infrared spectroscopy, and proton nuclear magnetic resonance were used to identify the phytoconstituents of the fraction.

Results Initial screening revealed fraction 2 (F2) as the most active fraction. Additionally, F2 showed the least cytotoxic effect on normal human fibroblast cells. Mechanistically, F2 induced cell cycle arrest and apoptosis in cervical cancer cells. F2 increased ROS levels, induced ER stress, and activated cell survival pathway. Treatment with N-acetyl cysteine revealed that F2 induced ROS-independent ER stress and apoptosis. 3D spheroid viability and growth delay experiments demonstrated the strong antitumor potential of F2. Finally, six compounds, including one flavonoid (nicotiflorin) and five limonoids, were identified in the F2 fraction.

Conclusion This is the first study to identify the active fraction and its phytoconstituents from neem stem bark and demonstrate the anticancer mechanism against cervical cancer. Our study highlights the importance

*Correspondence:
Jayasri Das Sarma
dassarmaj@iiserkol.ac.in
Full list of author information is available at the end of the article

© The Author(s) 2025. **Open Access** This article is licensed under a Creative Commons Attribution-NonCommercial-NoDerivatives 4.0 International License, which permits any non-commercial use, sharing, distribution and reproduction in any medium or format, as long as you give appropriate credit to the original author(s) and the source, provide a link to the Creative Commons licence, and indicate if you modified the licensed material. You do not have permission under this licence to share adapted material derived from this article or parts of it. The images or other third party material in this article are included in the article's Creative Commons licence, unless indicated otherwise in a credit line to the material. If material is not included in the article's Creative Commons licence and your intended use is not permitted by statutory regulation or exceeds the permitted use, you will need to obtain permission directly from the copyright holder. To view a copy of this licence, visit http://creativecommons.org/licenses/by-nc-nd/4.0/.

of investigating neem stem bark-derived limonoids and nicotiflorin as a potential source to develop new anticancer therapeutic agents.

Keywords *Azadirachta indica*, Cervical cancer, ER stress, Reactive oxygen species, 3D spheroids, Cell cycle arrest, Apoptosis

Graphical Abstract

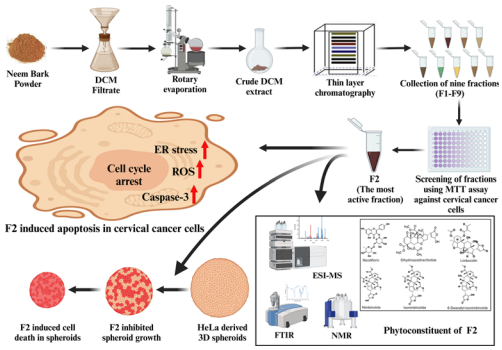

Introduction

Cervical cancer has remained a huge burden on women's health around the globe and, specifically, in Asian countries. In 2022, almost 662,301 cases were registered, and 348,874 deaths occurred due to cervical cancer globally. Among these, Asia reported more than 50% of cervical cancer-related incidence and mortality [1]. Due to poor screening and access to medical facilities in developing countries, the disease remains unnoticed till it reaches advanced stages [2, 3]. Treatment options for cervical cancer include surgery, chemotherapy, and radiotherapy, which may be used independently or in combination, depending on the disease stage. However, there has not been any significant improvement in the survival of cervical cancer patients owing to disease recurrence, chemotherapeutic resistance, and treatment-associated side effects [4]. Hence, it is essential to investigate and develop new therapeutic drugs to efficiently treat cervical cancer patients and improve their quality of life.

Natural products are under constant investigation as they encompass numerous biologically active compounds of value to medicine. The high structural diversity and therapeutic potential of compounds derived from natural products serve as building blocks for developing more efficient drugs [5]. Phytoconstituents of *Azadirachta indica* A. Juss. (Neem) represents a wide range of biologically active compounds now known for their chemopreventive, chemosensitizing, and antitumorigenic properties [6–8]. Extensive research has been done to study the therapeutic efficacy of extracts prepared from different parts of the neem tree, including leaf, seed, and flower [9, 10]. Moreover, numerous bioactive compounds with anticancer activity have been isolated from neem leaves, seeds, or flowers, which include nimbolide, gedunin, azadirachtin, nimbin, quercetin, etc. Their anticancer mechanism involves disruption of oncogenic signaling pathways, activating unfolded protein response (UPR), cell cycle arrest, activation of intrinsic and extrinsic apoptotic pathways, induction of DNA damage, and inhibition of metastasis [7–9].

Very early reports showed the antitumor efficacy of neem bark derived polysaccharides against the murine sarcoma model [11]. Recently, our laboratory has demonstrated the anticancer potential of neem bark extract against cervical cancer [12]. Interestingly, another group reported the antineoplastic activity of silver nanoparticles synthesized using neem bark extract against prostate cancer cells [13]. However, the precise mechanism and the bioactive compounds responsible for the anticancer potential of neem bark extract are yet to be investigated. Considering the significant archive of information available in the traditional and scientific literature on the anticancer potential of neem bark, this study aimed to further identify the active constituents of neem bark extract and to explore the underlying anticancer mechanism using in vitro 2D cultured cervical cancer cells and 3D cervical tumor spheroids.

Materials and methods

Preparation and fractionation of the extract

Dr. Bhargav's neem bark powder was purchased from Amazing Herbals (Cat. No. Nmbp02, Batch No.

NBP-101, Bhargav's Enclave, Haryana, India). The extraction and fractionation from neem stem bark powder was done as described previously [14]. Briefly, 100 g of Dr. Bhargav's neem bark powder was soaked in 1000 mL of low-polar solvent DCM for 24 h at room temperature (RT). The extract was then filtered through a Whatman No. 42 (125 mm) filter paper, and the filtrate was concentrated using a vacuumed rotary evaporator. The resulting neem bark extract was collected and stored in a cool and dry place. The obtained DCM crude extract was fractionated by TLC using silica gel G. A fine glass capillary tube was used to spot samples accurately onto the TLC plate, aiming for precise and small spots to enhance resolution. Then, the plate was inserted in a glass chamber using 100 mL DCM solvent. After completion, the TLC plate was carefully removed from the chamber, and the solvent front was marked, followed by visualization of the spots with UV light. This process led to the separation of the extract into nine fractions labeled F1-F9. The fractions were collected by passing the extract through a glass chromatography column with a PTFE stopcock using DCM as the solvent. The solvent was then evaporated by a rotary vacuum evaporator. The obtained powder was dissolved in Dimethyl sulfoxide (DMSO; cell-culture grade) at a concentration of 100 mg/mL. The extract was filtered through a 0.22 µm membrane filter and stored in the freezer at −20 °C until use. In all the experiments, DMSO was used as vehicle control, and concentration did not exceed 0.4%.

Cell culture

Human cervical cancer cell lines, HeLa (CRM-CCL-2) and ME-180 (HTB-33), human lung cancer cell line A549 (CCL-185), human liver cancer cell line Hep G2 (HB-8065), and non-tumorigenic human fibroblast cell line HFF-1 (SCRC-1041) were purchased from ATCC. Mouse glioma cell line CT-2 A (SCC194) was purchased from Sigma-Aldrich. HeLa, A549, CT-2 A, Hep G2, and human fibroblast cells were cultured in DMEM and ME-180 cells in RPMI-1640, supplemented with 10% fetal bovine serum (FBS) and 1% penicillin/streptomycin. All cells were cultured at 37 °C in a humidified incubator with 5% CO2. All cell culture reagents were purchased from GIBCO.

Cell viability assay

As described previously, 3-(4,5-dimethylthiazol-2-yl)−2,5-diphenyltetrazolium bromide (MTT) assay was used to identify the fraction with the highest anticancer activity [12]. Briefly, cells were seeded at a density of 10^4 cells/well in 96-well plates (Nunc, Denmark) and incubated overnight. After incubation, cells were exposed to different doses of fractions (0–300 µg/mL) for 24 h. After 24 h, the cell viability was measured using MTT (Sigma Aldrich). Absorbance was measured at 570 nm in the BioTek Epoch microplate reader. Each dose was assessed in triplicates. The cytotoxic effect of fractions was expressed as the percentage of viable cells in comparison to vehicle control. The dose-response curve using [inhibitor] vs. response-variable slope (four parameters) was created by GraphPad Prism 8.0 (GraphPad Software, San Diego, CA, USA). As F2 showed the highest growth inhibitory effect, the concentration of the F2 inhibiting cell growth by 25% (IC_{25}) and 50% (IC_{50}) was used for further studies.

Clonogenic assay

Approximately 500 HeLa and ME-180 cells were plated in 60 mm dishes (Nunc, Denmark) and incubated overnight. Cells were treated with vehicle or F2 at their respective IC_{25} and IC_{50} dose or vehicle and incubated further for 24 h. After 24 h, cells were maintained in a fresh culture medium for 10–14 days for colony formation. Cells were then fixed with 4% paraformaldehyde and stained with 0.4% crystal violet. Colonies with at least 50 cells were considered. Survival fraction was calculated as the ratio of the number of colonies formed after treatment to the number of cells seeded and normalized with plating efficiency (PE: number of colonies formed by vehicle control/number of cells seeded) [15]. All treatments were performed in triplicate, and the experiment was repeated three times.

Cell cycle analysis

HeLa and ME-180 cells were seeded in 6-well plates (3×10^5 cells/well) in their respective culture medium and incubated overnight. The cells were exposed to F2 at their respective IC_{25} and IC_{50} dose or vehicle for 24 h. After 24 h, cells were harvested and washed with ice-cold PBS. Cells were fixed in 70% ethanol, washed with ice-cold PBS twice, and incubated in PBS containing 50 µg/mL propidium iodide (PI), 0.05% Triton X-100, and 100 µg/mL RNase A solution (Thermo Scientific) for 30 min at RT in the dark, followed by flow cytometric analysis (BD FACSVerse; BD Biosciences) [12]. Cell cycle distribution (G_1/G_0, S, and G_2/M) was determined using FlowJo software (version 10.7.1).

Apoptosis assay

F2 induced apoptosis was determined using Annexin V-FITC/PI staining. HeLa and ME-180 cells were collected after treatment with F2 and stained according to the manufacturer's protocol (eBioscience™ Annexin V-FITC Apoptosis Detection Kit Cat. No. BMS500FI). The data was acquired within one hour by flow cytometry (BD FACSVerse; BD Biosciences). Data were analyzed

in FlowJo software. The experiment was performed in triplicates and repeated thrice.

Active caspase-3 expression analysis

Active caspase-3 expression was analyzed using indirect intracellular flow cytometry [12]. Following treatment with F2, cells were harvested, fixed, and permeabilized using BD Cytofix/Cytoperm Kit. Permeablized cells were incubated with anti-active-caspase-3 (1:250, BD Biosciences; 559565) antibody for 30 min at RT. Cells were washed thrice and incubated with APC-conjugated (Allophycocyanin) goat anti-rabbit antibody for 30 min at RT. Cells stained with only APC-conjugated antibody was used as a negative control. The stained cells were analyzed by flow cytometry (BD FACSVerse; BD Biosciences). Data were analyzed in FlowJo software. The experiments were performed in duplicates and repeated thrice.

Quantification of ROS

2′,7′-Dichlorofluorescin diacetate (Sigma) was used as ROS indicator. After F2 treatment, cells were washed with warm PBS and incubated with 5 µM dye prepared in serum-free media for 30 min in a CO_2 incubator at 37 °C. Cells were harvested, resuspended in PBS, and immediately taken for data acquisition in a BD FACSVerse flow cytometer. Data were analyzed in FlowJo software. The experiments were performed in duplicates and repeated thrice.

RNA isolation and quantitative real-time PCR

Approximately 1×10^6 cells were seeded in 60 mm dishes and treated with F2 at their respective IC_{25} and IC_{50} doses for 24 h. After 24 h, cells were washed with ice-cold PBS. RNA extraction, cDNA preparation, and real-time PCR were performed as described previously [12, 16]. Glyceraldehyde-3-phosphate dehydrogenase (GAPDH) was used as an internal control, and relative expression was quantified using the formula $2^{-\Delta\Delta Cq}$. The primer pairs used are listed in the supplementary information II, Table S2.1.

Protein extraction and Western blot

HeLa and ME-180 cells were treated with F2 at IC_{25} and IC_{50} doses for 24 h. After treatment, cells were collected in RIPA buffer containing protease and phosphatase inhibitor cocktail and incubated for 45 min on ice. Lysate was centrifuged at 12 000 g for 15 min at 4ºC, and the supernatant was collected. Pierce® BCA protein assay kit (Thermo Scientific) was used to determine protein concentration. Western blot was performed as described in our previous study [12]. Primary antibody against Bax (1:1000, BioBharati; BB-AB0250), GRP78 (1:1000, CST; 3177), P-PERK (Thr982) (1:1000, Affinity Biosciences; DF7576), P-eIF2α (Ser52) (1:1000, Invitrogen; 44-728G), P-Akt (Ser473) (1:1500, CST; 4060), and GAPDH (1:5000, BioBharati; BB-AB0060) were used. Protein expression was analyzed using Image J software. Protein expression levels of target genes were normalized to GAPDH gene expression and expressed as relative fold change compared to vehicle control. Samples were loaded in duplicates, and the experiments were repeated three independent times. Full uncropped blots are provided in the supplementary information I.

3D HeLa spheroid generation

The hanging drop method was used to generate HeLa cell-derived 3D spheroids [17]. Briefly, a single-cell suspension was prepared such that a 20 µL drop contains 3×10^3 cells. HeLa cells were then plated as 20 µL droplets onto the cap of 60 mm dishes. The cap was captured upside down on top of the dish prefilled with 4 mL of PBS and then incubated for 4 days in a CO_2 incubator. The liquid overlay culture technique was utilized to further enhance the size of spheroids. Spheroids were transferred to a 96-well flat bottom plate precoated with 50 µL of 1.5% agarose and incubated in a CO_2 incubator. Spheroids usually acquired 300 µm size after 2 days in agarose-coated plates.

Acid phosphatase assay

Spheroid viability was determined as described previously [18]. Spheroids with sizes between 250 and 300 µm were treated with different doses of F2 (0–200 µg/mL) and incubated for 72 h. Spheroids were then transferred to a 96-well flat bottom plate and centrifuged at 400 g for 10 min at RT. Spheroids were washed with PBS twice and incubated with 100 µL of APH assay buffer (0.1 M sodium acetate, 0.1% Triton-X-100, and 5 mM p-nitrophenyl phosphate, final pH 4.8) for 90 min at 37 °C. Following incubation, 10 µL of 1 N NaOH was added to each well, and absorbance was taken at 405 nm within 10 min. Each dose was assayed with a minimum of seven replicates and repeated twice.

Hoechst and PI staining

Following treatment with F2, spheroids were stained with Hoechst 33,342 and PI at a final concentration of 10 µM. Dyes were prepared in PBS and added directly to the culture medium, followed by incubation at 37 °C for 30 min in a CO_2 incubator. Following incubation, spheroids were washed with PBS and imaged using a BioTek Cytation5 multimode plate reader. The z-stack images of each spheroid were captured with the 10X objective across the entire spheroid thickness using DAPI (360/460 nm) and Texas Red (535/617 nm) filter settings for simultaneous

dual-channel recordings; approximately 70 z-stacks with a step size of 5 µm per spheroid were taken. Z-stacks were processed using the BioTek Gen5 software and presented as a maximum intensity projection image.

Spheroid growth delay analysis

Spheroids with a size between 250 and 300 µm were treated with 0–100 µg/mL of F2 for 72 h. Phase contrast images of spheroids before and after 72 h of treatment with F2 were collected with an inverted Nikon Eclipse Ts2 microscope (4X) (Tokyo, Japan). After 72 h and every 48 h thereafter, 50% of the media was replaced with a fresh culture medium, and images were captured. Images were analyzed with ImageJ software using a macro described previously [19]. The spheroid area (A) measured with the help of macro was analyzed in Excel and used to calculate the radius ($R= \sqrt{(A/\pi)}$) and volume of the spheroid ($V=4/3\ \pi r^3$). Fold change in spheroid volume was calculated as the ratio of the difference between initial spheroid volume and final spheroid volume over initial spheroid volume.

Identification of bioactive compounds

For the identification of compounds in F2, Mass spectra (ESI-MS) were recorded in positive mode electrospray ionization using a Xevo G2-XS QTof mass spectrometer. Molecular details about neem compounds were collected from the database Indian Medicinal Plants, Phytochemistry and Therapeutics (IMPPAT, https://cb.imsc.res.in/imppat/) and Bio-activity Informatics of Indian Medicinal Plants (BIMP, http://www.scfbio-iitd.res.in/plants_scf/search_neem1.html). FTIR spectra were recorded with a PerkinElmer instrument, preparing a pellet with sample and KBr at RT by averaging 30 scans. Background spectra were deducted from each sample spectrum. ^{1}H NMR spectra were recorded using a Bruker-500 spectrometer. Chemical shifts were reported in parts per million (δ) relative to $CDCl_3$ (7.26 ppm for ^{1}H as an internal reference).

Statistical analysis

Unless otherwise stated, all experiments were performed at least three independent times, and data are presented as mean ± SEM. One-way ANOVA followed by Dunnett's and Tukey's Multiple Comparison Tests were performed to determine the significance of differences between vehicle control and all treatment groups and among groups, respectively. All statistical analyses were done using GraphPad (La Jolla, CA) Prism 8. A P value of < 0.05 was considered statistically significant.

Results

F2 demonstrated a strong antiproliferative effect, specifically on cervical cancer cells

Nine fractions (F1-F9) were obtained after fractionation of DCM extract of neem bark using TLC. HeLa and ME-180 cervical cancer cell lines were exposed to various doses of the respective fractions (0–300 µg/mL) for 24 h. Cell viability assay revealed that all fractions decreased the cell viability of both cell lines in a dose-dependent manner. However, among all the fractions, F1-F4 exhibited a strong growth inhibitory effect against HeLa (Fig. 1A) and ME-180 cells (Fig. 1B) as compared to F5-F9 (supplementary information II, Fig. S2.1). Among F1-F4, F2 was found to be the most active fraction with an IC_{50} dose of 91 µg/mL for HeLa and 33 µg/mL for ME-180. Apart from cervical cancer cells, F2 showed dose-dependent inhibition on the growth of other cancer cell types, including lung cancer, glioma, and hepatic cancer, demonstrating its strong anticancer potential (supplementary information II, Fig. S2.2). However, the anticancer effect was more pronounced against cervical cancer cells.

Additionally, as shown in Fig. 1C, F2 had a minimal effect on the growth of normal human fibroblast cells, which implies the specificity of F2 toward cancer cells. Since F2 showed the highest cytotoxicity among different fractions, it was considered further to evaluate its anticancer potential against cervical cancer. In all the successive experiments, HeLa and ME-180 were treated with F2 at their respective IC_{25} and IC_{50} doses.

Clonogenic assay was employed to validate the antiproliferative effect of F2. Clonogenic assay determines the proliferative capacity and survival ability of cancer cells after drug exposure. As shown in Fig. 1D, F2 significantly reduced the survival of HeLa and ME-180 cells by more than 50% at their respective IC_{25} dose and more than 95% at their respective IC_{50} dose compared to vehicle control. In addition to colony number, colony size was also reduced compared to vehicle control.

F2 induced S and G2/M phase arrest and downregulated the expression of cell cycle related genes

Cell cycle analysis was performed to investigate the mechanism behind the growth inhibitory potential of F2. As shown in Fig. 2A, cell cycle analysis revealed that treatment with F2 at IC_{25} and IC_{50} dose arrested HeLa cells at S and G_2/M phase compared to vehicle control. Similarly, exposure of ME-180 cells to F2 at IC_{25} and IC_{50} dose promoted S-G_2/M phase and G_2/M phase arrest, respectively, compared to vehicle control. The treatment concomitantly decreased the number of cells in the G_0/G_1 phase in both cell lines.

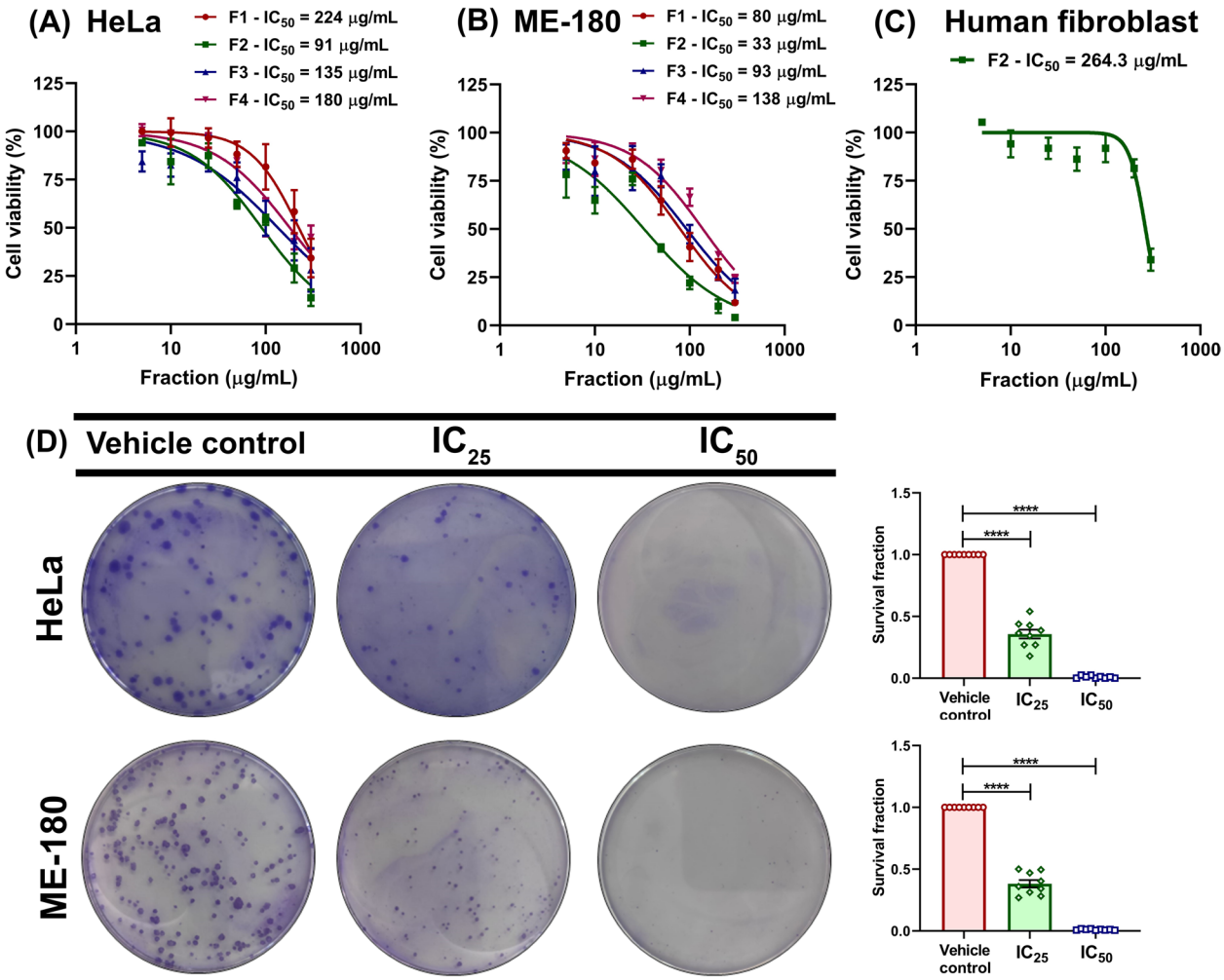

Fig. 1 Anticancer screening of dichloromethane fractions of neem bark revealed F2 as the most active fraction. Effect of F1-F4 fractions on the viability of (**A**) HeLa and (**B**) ME-180 cells measured by MTT assay after 24 h treatment. **C** Effect of F2 on viability of normal human fibroblast cells after 24 h treatment. **D** Representative images of clonogenic assay performed using HeLa and ME-180 cells after 24 h treatment with F2. The bar graph represents the quantification of colony formation compared to vehicle control, which is expressed as the survival fraction. All experiments were performed in triplicate, and data are expressed as the mean ± SEM of the three independent experiments. Vehicle-treated cells were used as control. **** $P < 0.0001$ vs. vehicle control

Furthermore, we examined the mRNA expression of S and G_2/M phase related genes (cyclin A, cyclin B, and *CDK1*) after treatment with F2. As shown in Fig. 2B, F2 significantly decreased the levels of cyclin A in HeLa cells in a dose-dependent manner. However, there was no change in the expression of cyclin B and *CDK1*. In the case of ME-180 cells, there was a significant reduction in levels of cyclin A, cyclin B, and *CDK1* at the IC_{50} dose. Taken together, results suggest that the suppression of cell cycle regulatory genes by F2 might be responsible for the abrogation of the cell cycle in HeLa and ME-180 cells.

F2 promoted apoptosis and upregulated caspase-3 in cervical cancer cells

Treatment of HeLa and ME-180 cells with F2 at IC_{25} and IC_{50} doses significantly induced early- and late-stage apoptosis compared to vehicle control (Fig. 3A). To further confirm the F2-induced apoptosis, we evaluated the expression of pro-apoptotic proteins, active-caspase-3, and BAX. We also analyzed the mRNA expression of the anti-apoptotic gene survivin. As shown in Fig. 3B, the expression of active-caspase-3 increased dose-dependently in both the cell lines after treatment with F2 for 24 h. We also observed an

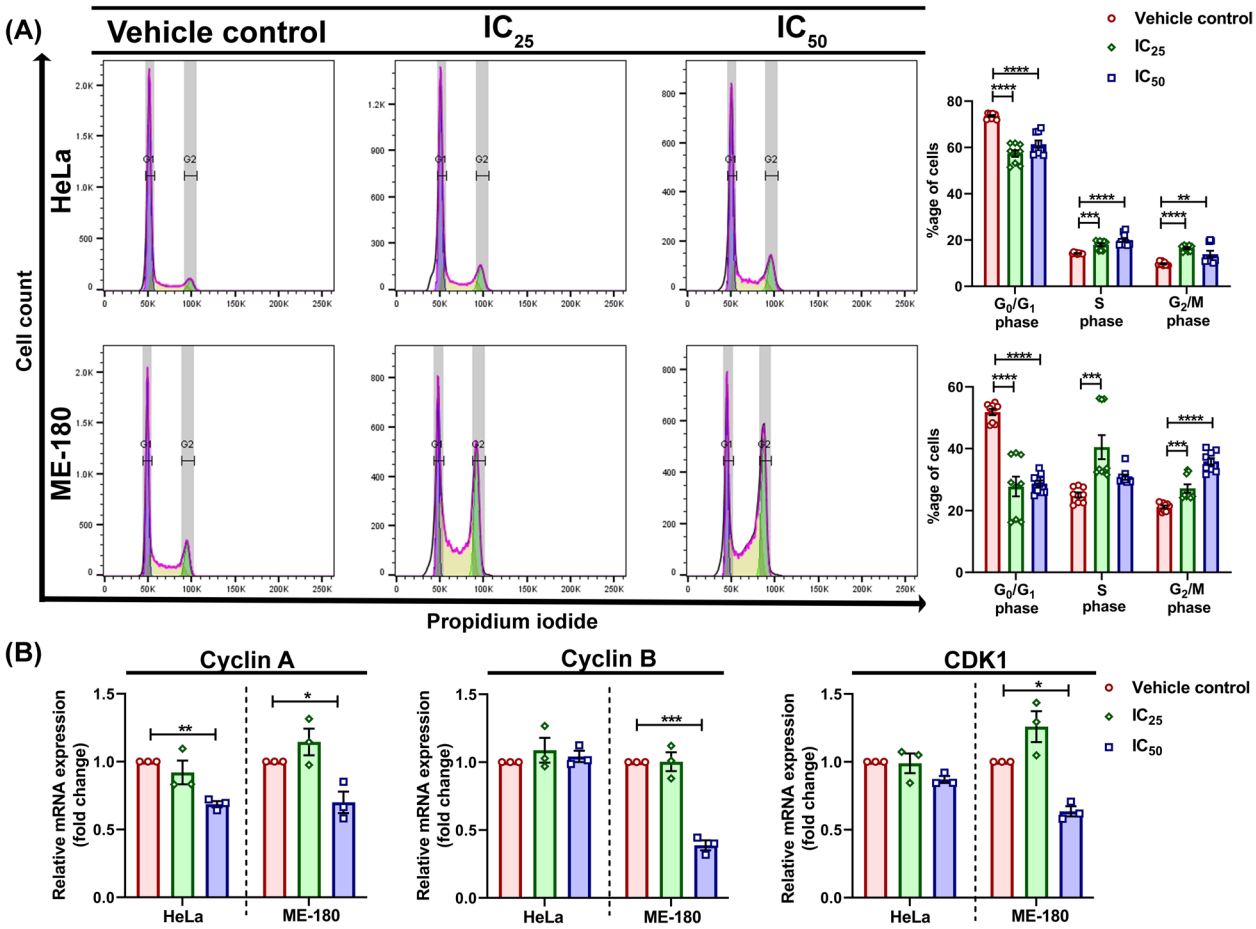

Fig. 2 F2 induces S and G_2/M phase arrest in HeLa and ME-180 cells. **A** Distribution of HeLa and ME-180 cells in various phases of the cell cycle after treatment with F2 for 24 h, analyzed using flow cytometry. **B** mRNA expression analysis of cyclin A, cyclin B, and *CDK1* after cells were treated with F2 for 24 h. Data expressed as the mean ± SEM of the three independent experiments. Vehicle-treated cells were used as control. The significant differences from control are indicated by **P* < 0.05, ***P* < 0.01, ****P* < 0.001, and*****P* < 0.0001 vs vehicle control

upregulation in the expression levels of BAX after F2 treatment (Fig. 3C). Additionally, we evaluated the transcript levels of survivin, whose product is responsible for increasing cell survival by inhibiting the activity of pro-apoptotic enzyme caspase-9 [20]. As shown in Fig. 3D, we found a dose-dependent downregulation of survivin at the transcriptional level in ME-180 cells. In contrast, there was no change in mRNA levels of survivin in HeLa cells. Altogether, the data suggest that F2 induces cell death by regulating the expression of pro- and anti-apoptotic proteins.

F2 triggered ROS production and regulated UPR and cell survival-related proteins in cervical cancer cells

To further understand the molecular mechanisms by which F2 induces cell death in cervical cancer cells, we examined the ROS levels and expression of critical signaling proteins associated with ER stress and cell survival.

(See figure on next page.)

Fig. 3 F2 induces apoptosis in cervical cancer cells. **A** Apoptotic cell analysis of F2 treated HeLa and ME-180 cells by flow cytometry using Annexin V–FITC and PI staining. Bar diagrams represent the percentage of early, late, and total apoptosis calculated by FlowJo software. **B** Protein expression analysis of active caspase-3 analyzed by flow cytometry in HeLa and ME-180 cells after a 24 h treatment with F2. **C** Western blot analysis of the expression of BAX in HeLa and ME-180 cells treated with F2 at the indicated dose for 24 h. GAPDH was employed as a loading control. Uncropped blots are provided in the supplementary information I, Figure S1.1. **D** Real-time PCR analysis of survivin after cells were treated with F2 for 24 h. Data expressed as the mean ± SEM of the three independent experiments. Vehicle-treated cells were used as control. The significant differences from control are indicated by **P* < 0.05, ***P* < 0.01, ****P* < 0.001, and *****P* < 0.0001 vs. vehicle control

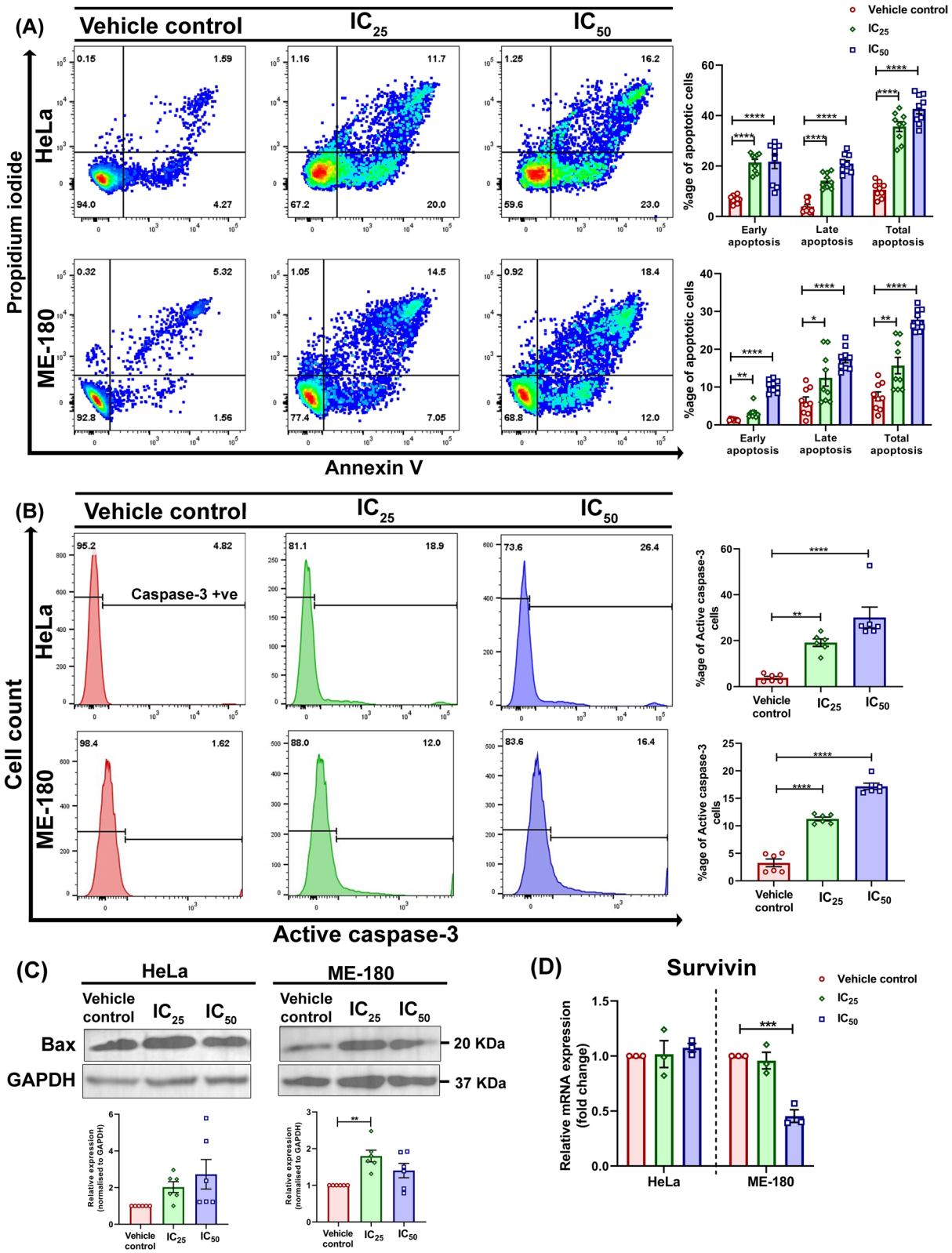

Fig. 3 (See legend on previous page.)

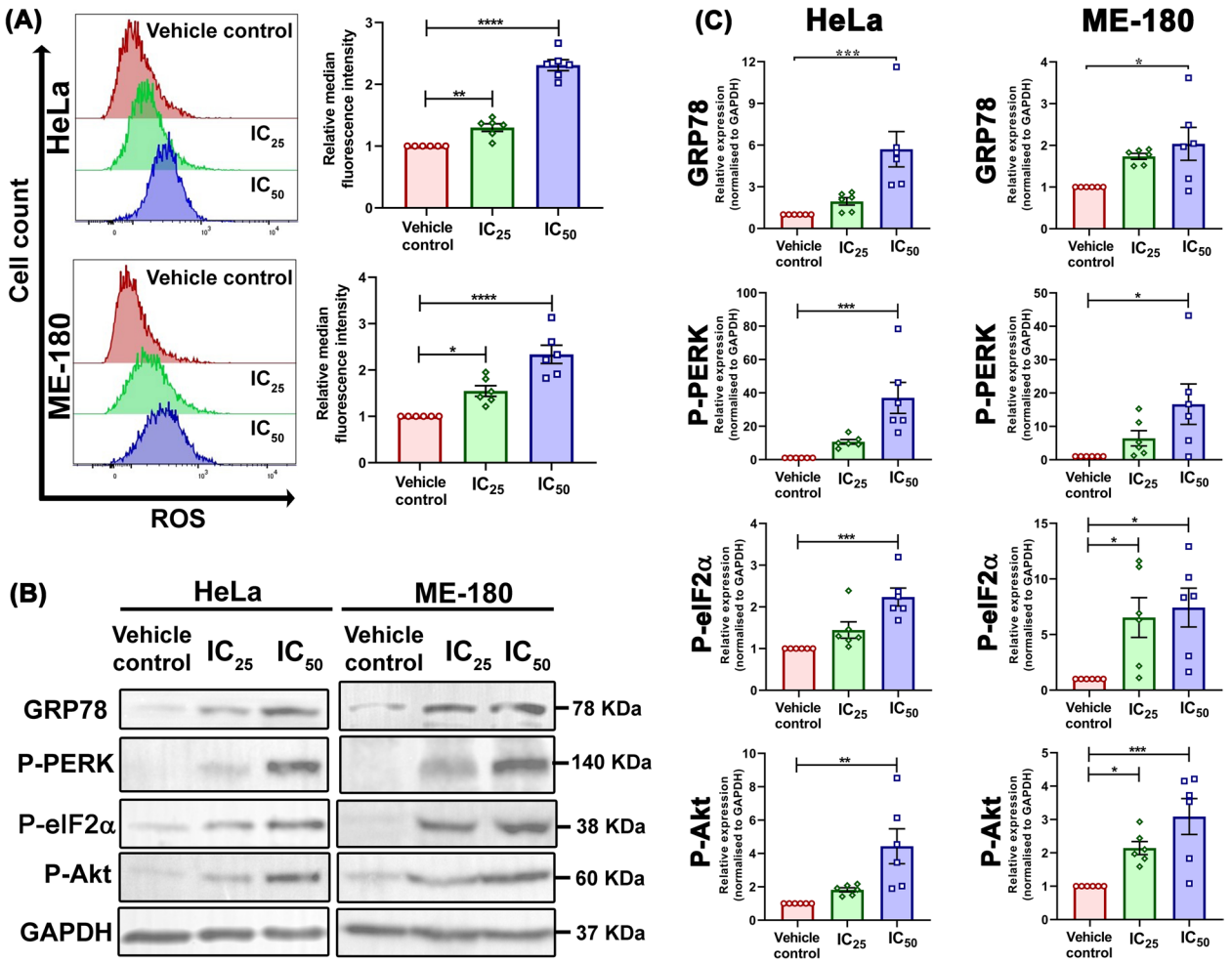

Fig. 4 F2 increases ROS levels, induces ER stress, and activates the cell survival pathway in cervical cancer cells. **A** ROS levels in F2 treated HeLa and ME-180 cells were assessed using 2′,7′-Dichlorofluorescin diacetate probe followed by flow cytometry. The bar graph represents the relative median fluorescence intensity of cells compared to vehicle control. **B** Representative western blots and (**C**) densitometric analysis of the expression of GRP78, P-PERK (Thr982), P-eIF2α (Ser52), and P-Akt (Ser473) in HeLa and ME-180 cells treated with F2 at indicated dose for 24 h. GAPDH was used as a loading control. Uncropped blots are provided in the supplementary information I, Figure S1.2-S1.4. Data expressed as the mean ± SEM of the three independent experiments. Vehicle-treated cells were used as control. The significant differences are indicated by $^{*}P < 0.05$, $^{**}P < 0.01$, $^{***}P < 0.001$, and $^{****}P < 0.0001$ vs. vehicle control

As shown in Fig. 4A, treatment of HeLa and ME-180 cells with F2 at IC_{25} and IC_{50} dose for 24 h resulted in a significant increase in ROS levels compared to vehicle control, and the elevation in ROS level was dose-dependent.

It is well known that increased levels of ROS can induce ER stress and UPR activation in cancer cells. Therefore, we analyzed the expression of ER stress markers after F2 treatment. As shown in Fig. 4B and C, the expression of ER stress markers, including GRP78, P-PERK, and P-eIF2α, significantly increased after F2 treatment in both HeLa and ME-180 cells, confirming the activation of the UPR pathway. We further assessed the activation status of protein kinase B (Akt) as it is essential for cell survival under stress conditions. We found that F2 treatment led to a significant increase in the expression of phosphorylated Akt in a dose-dependent manner (Fig. 4B and C). Thus, overall, the results indicate that F2 treatment causes an increase in ROS levels and activation of ER stress and cell survival pathways.

NAC enhanced the F2 mediated cytotoxicity against cervical cancer cells

To determine if the ER stress induction and apoptosis in F2 treated cells were dependent on ROS generation, we used a ROS scavenger NAC. We pretreated the cells with NAC at 10 mM dose for 1 h, followed by the

addition of F2 for 24 h. Unexpectedly, we found that NAC failed to restore the cell viability and, in fact, significantly increased the anti-cancer effect of F2 against HeLa and ME-180 cells (Fig. 5A). On analyzing the ROS levels, we found that NAC treatment did not have any effect on F2 generated ROS levels in HeLa cells, however, NAC significantly reduced the ROS levels in ME-180 cells (Fig. 5B and C).

Additionally, there were no significant changes in the expression levels of GRP78, P-PERK, and P-eIF2α in both cell lines, suggesting that induction of ER stress was independent of ROS generation (Fig. 6A and B). Surprisingly, NAC treatment downregulated the expression of F2 activated Akt, which might explain the NAC mediated enhancement of F2 induced cell death (Fig. 6C and D).

F2 dose-dependently reduced the viability and growth of 3D HeLa spheroids

The potency of F2 against spheroids was measured by APH assay. As shown in Fig. 7A, treatment of spheroids with increasing dose (0–200 µg/mL) of F2 for 72 h suppressed the viability in a dose-dependent manner. To further validate our results, we stained the spheroids with Hoechst and PI to visualize the cell death within the spheroids. As expected, we found a dose-dependent increase in the PI staining (an indicator of cell death) compared to vehicle control (Fig. 7B), confirming the anti-tumor potential of F2. We further aimed to determine the effect of F2 treatment on the survival of spheroids by analyzing the spheroid growth kinetics for 15 days post-treatment. As shown in Fig. 7C, we observed regrowth only

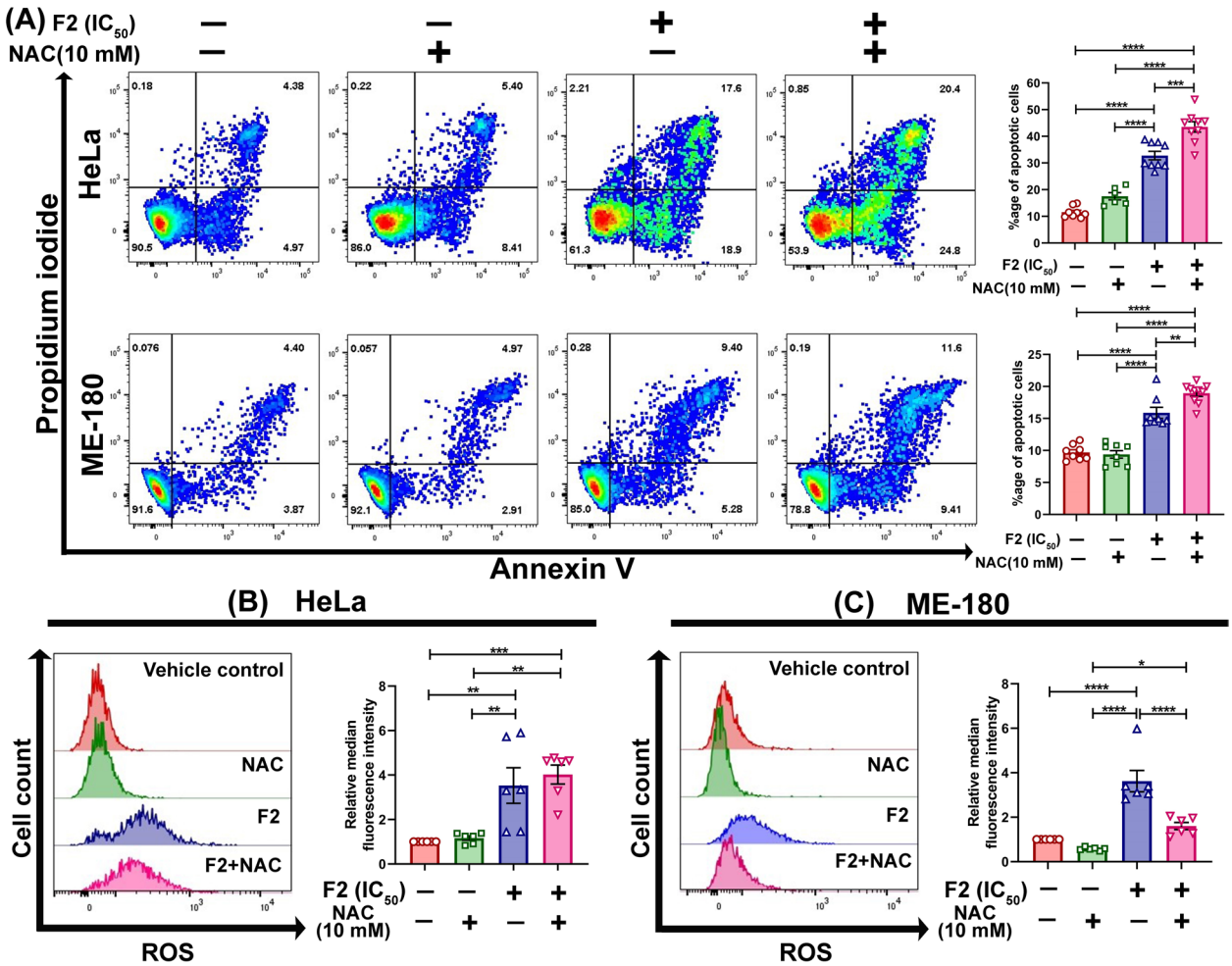

Fig. 5 Co-treatment with NAC enhances the apoptotic potential of F2. HeLa and ME-180 cells were treated with F2 in the presence or absence of ROS inhibitor NAC for 24 h. **A** Cell death was assessed using Annexin V-FITC and PI staining, and ROS levels were measured in (**B**) HeLa and (**C**) ME-180 cells using 2′,7′-Dichlorofluorescin diacetate staining followed by flow cytometry. Data expressed as the mean ± SEM of the three independent experiments. Vehicle-treated cells were used as control. The significant differences are indicated by $*P < 0.05$, $**P < 0.01$, $***P < 0.001$, and $****P < 0.0001$

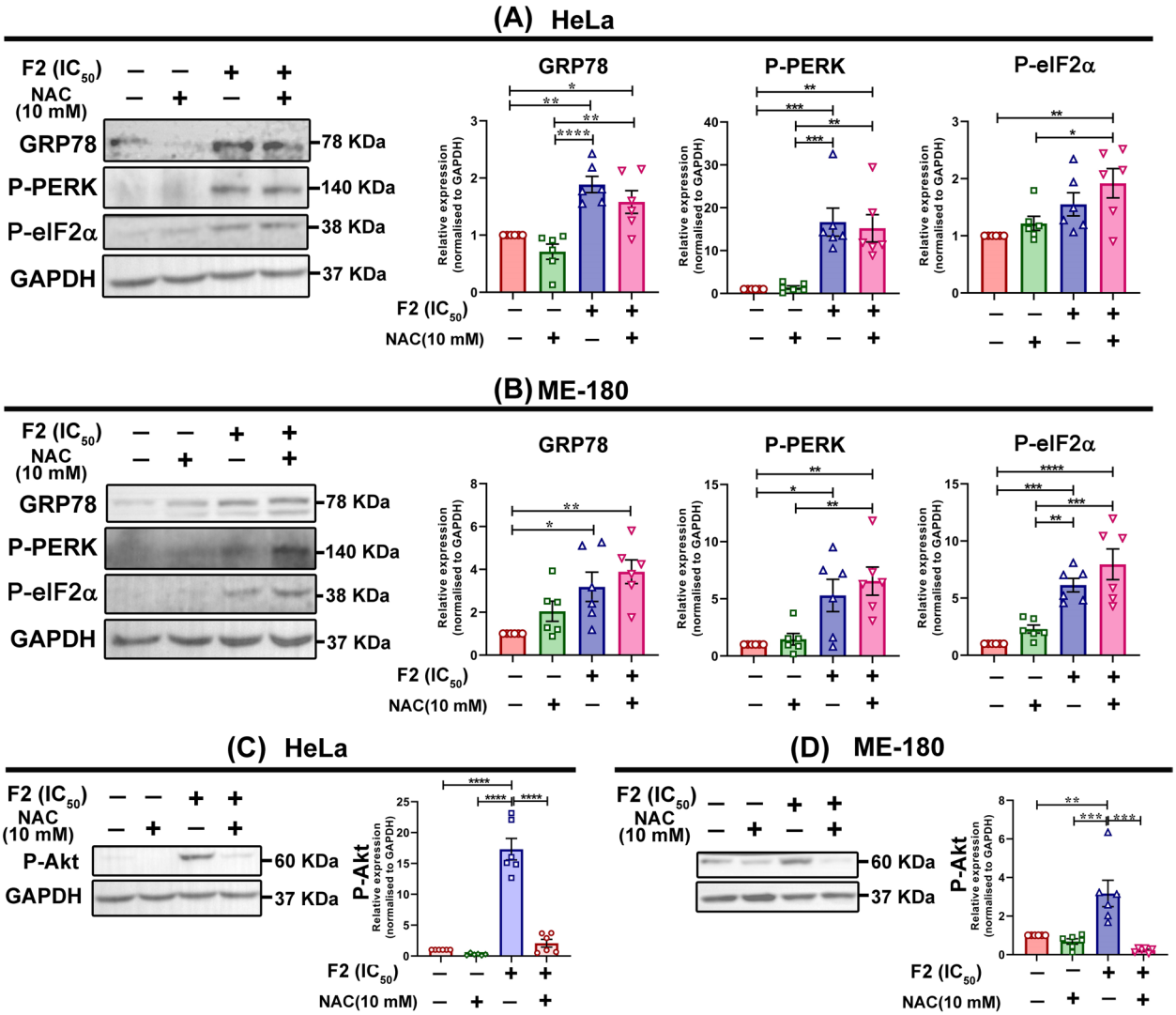

Fig. 6 F2 induces ROS-independent ER stress in cervical cancer cells. Immunoblot analysis of ER stress markers, including GRP78, P-PERK (Thr982), and P-eIF2α (Ser52) in (**A**) HeLa and (**B**) ME-180 cells after co-treatment with F2 and NAC for 24 h. P-Akt (Ser473) levels were analyzed by immunoblotting in (**C**) HeLa and (**D**) ME-180 cells after co-treatment with F2 and NAC for 24 h. GAPDH was used as a loading control. Uncropped blots are provided in the supplementary information I, Figures S1.5 and S1.6. Data expressed as the mean ± SEM of the three independent experiments. Vehicle-treated cells were used as control. The significant differences are indicated by $^{*}P < 0.05$, $^{**}P < 0.01$, $^{***}P < 0.001$, and $^{****}P < 0.0001$

in spheroids treated with F2 at 12.5 µg/mL dose on day 9 post-treatment. In contrast, spheroids treated with F2 at a dose of 25, 50, and 100 µg/mL did not show any sign of growth, demonstrating the strong potential of F2 as a candidate to develop new anticancer agents.

Identification of bioactive compounds in F2

F2 was further characterized by analytical techniques, including ESI-MS, FTIR, and ^{1}H NMR, to identify the compounds present in the fraction. ESI-MS analysis of F2 led to the identification of six compounds. Except for nicotiflorin, which is a flavonoid, the other five compounds, namely dihydroazadirachtolide, nimbinolide, isonimbinolide, 6-deacetyl-isonimbinolide, limbocidin, belong to a class of limonoids (Fig. 8). The mass spectrum of F2 is provided in the supplementary information II, Fig. S2.3. The molecular formula, ion fragmentation, and *m*/*z* value data of all molecules in F2 are provided in the Supplementary information II, Table S2.2. FTIR analysis of F2 confirmed the presence of functional groups including -C-H, -O-H, -C=O (supplementary information II, Fig. S2.4). Finally, ^{1}H NMR spectroscopy in

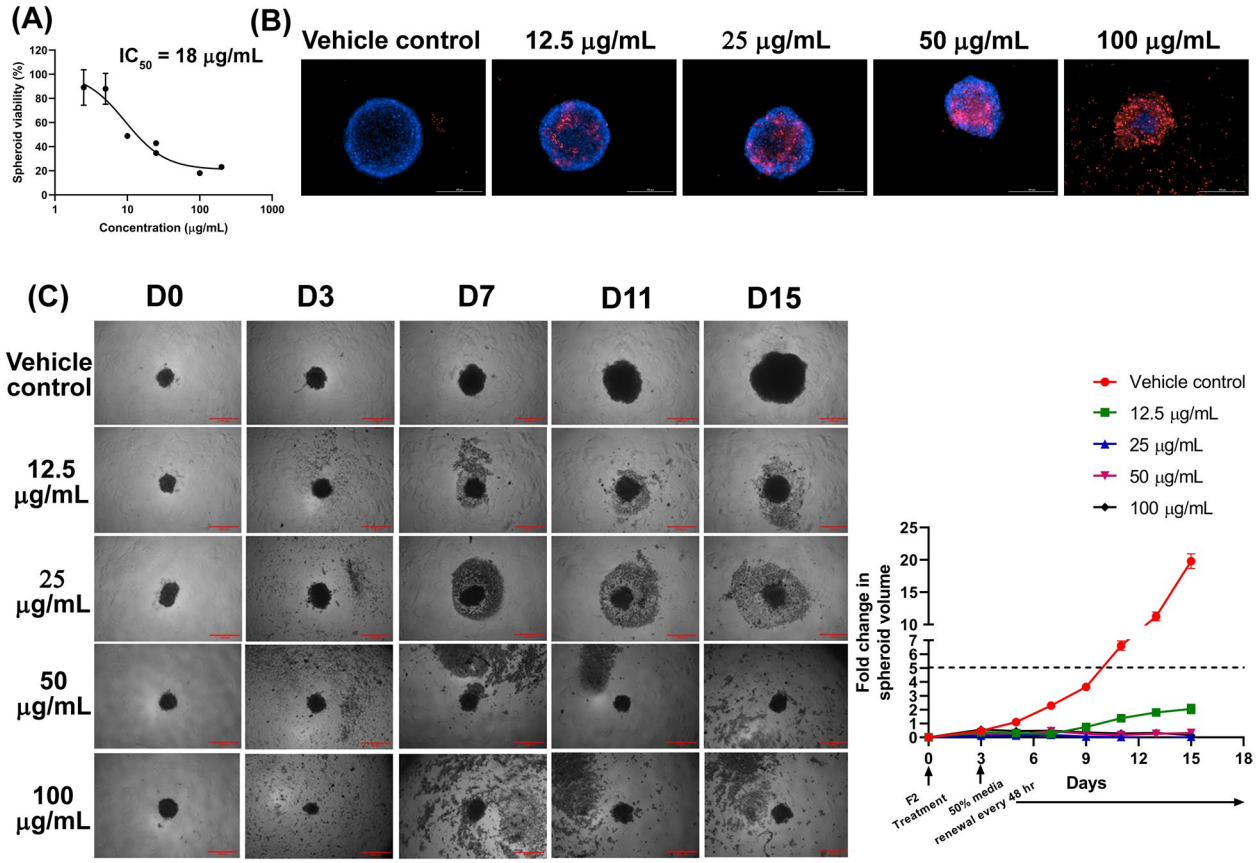

Fig. 7 F2 reduces the viability of HeLa spheroids and delays spheroid growth. HeLa cells derived spheroids were treated with increasing doses of F2 for 72 h. **A** The viability of spheroids was measured using acid phosphatase assay. The experiment was repeated twice. **B** Fluorescence microscopy images of spheroids stained with Hoechst (blue) and PI (red, dead cells) captured using BioTek Cytation5 multimode reader with 10X objective. "Maximum intensity projection image" of the spheroids generated from 70 z-stacks using Gen5 software. Scale bar 200 µm. The experiment was repeated thrice. **C** Representative bright field images of spheroids before and 72 h post-treatment with F2 and at an interval of 2 days thereafter till 15 days. Scale bar 1000 µm. The graph represents the fold change in the spheroid volume. The experiment was repeated twice. Data expressed as the mean ± SEM of independent experiments

$CDCl_3$ solvent was performed to understand the chemical environment and the position of hydrogen atoms of the compounds present in F2. By analyzing the ^1H NMR spectrum (supplementary information II, Fig. S2.5), the designated aliphatic (-CH_3, C-H), aromatic(-C-H), and O-H peaks of the compounds in the fraction were observed, which confirmed the presence of the mentioned compounds in F2.

Discussion

Over the past few years, phytotherapy has gained much attention for its therapeutic properties against multiple chronic diseases, including cancer. With the advancement in analytical techniques, a plethora of bioactive compounds with antineoplastic activity has been identified from several medicinal plants [5]. Among various medicinal plants, *Azadirachta indica* has remained a subject of interrogation due to its underexplored lurking potential to treat fatal diseases like cancer [7, 21]. Previously, we have reported that crude neem stem bark extract possesses anticancer potential and could induce apoptosis in cervical cancer cells [12]. However, the precise mechanism and the bioactive compounds responsible for the anticancer activity have not been assessed. Therefore, in this study, we further explored the therapeutic potential of neem stem bark extract and its underlying mechanism against cervical cancer. In the present study, we fractionated the neem stem bark extract in DCM using thin-layer chromatography and obtained nine fractions (F1-F9). Our initial screening performed against HeLa and ME-180 cells identified F2 as the most active fraction. Notably, the cytotoxicity of F2 against HeLa and ME-180 was even higher than that reported for crude neem bark extract previously [12]. Moreover, F2 showed relatively low cytotoxicity in normal human fibroblast cells compared to cervical cancer cells,

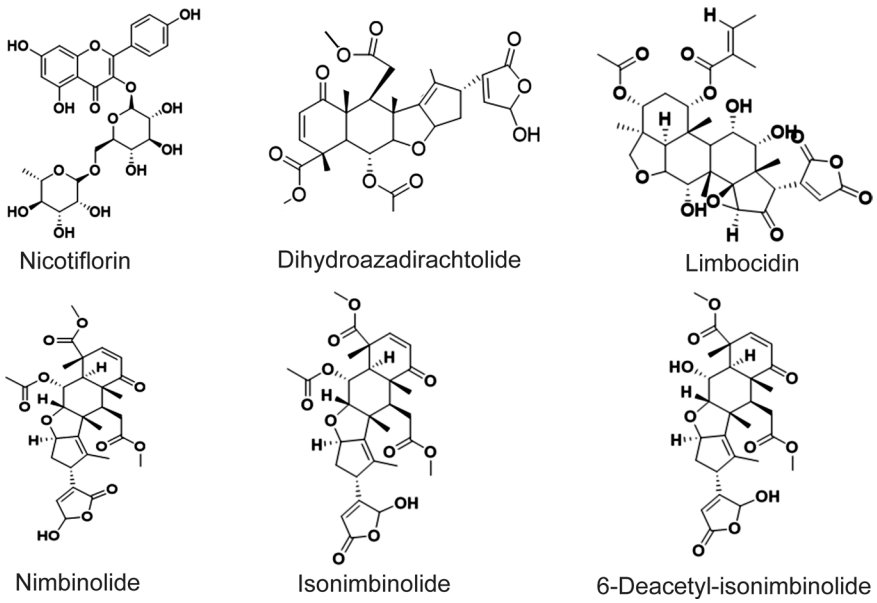

Fig. 8 Chemical structures of compounds identified in F2

emphasizing its safety towards normal cells. Altogether, the data demonstrated high therapeutic efficacy and safety of F2, which led us to further investigate its anticancer mechanism and identify the active components.

Cancer cells are known for their deregulated cell division and ability to evade apoptosis [22]. The results from the clonogenic assay showed a reduction in the number of colony formations and even in the colony size of cervical cancer cells after F2 treatment, which indicates the anti-proliferative and growth-suppressing potential of F2. From a mechanistic standpoint, F2 induced S and G_2/M phase arrest in HeLa and ME-180 cells by downregulating the expression of cyclin A in HeLa cells and cyclin A, cyclin B, and *CDK1* in ME-180 cells. Interaction of both cyclin A and cyclin B with *CDK1* is required to terminate the S phase and promote the entry of cells into the mitotic phase [23]. Hence, the depletion of such proteins abrogates the cell cycle progression, which might explain the growth-suppressing ability of F2 [24–26]. Additionally, Annexin V/PI staining revealed the strong potential of F2 to induce apoptosis in HeLa and ME-180 cells in a dose-dependent manner. Various chemotherapeutic drugs are known to induce apoptosis by modulating the expression of pro- and anti-apoptotic proteins, including Bcl2 family proteins, caspases, and members of the Inhibitor of apoptosis (IAP) family [27]. In fact, we observed downregulation of survivin (member of the IAP family) at mRNA level in F2 treated ME-180 cells as well as increased expression of pro-apoptotic proteins, BAX, and active caspase-3 in F2 treated HeLa and ME-180 cells, confirming the therapeutic potential of F2.

Numerous reports suggest that many phytochemicals trigger cancer cell death by inducing excessive ROS generation and ER stress [28, 29]. In fact, in our study, we found a significant increase in ROS levels in HeLa and ME-180 cells after F2 treatment. Additionally, several reports have also shown that ROS generation and ER stress are closely related, as excessive ROS levels can induce ER stress and vice-versa [28, 29]. Under ER stress, cancer cells activate the UPR pathway to restore ER homeostasis and maintain cell survival. However, prolonged or unresolved ER stress switches the UPR pathway toward apoptosis [30]. UPR pathway is mainly controlled by three proteins: inositol requiring enzyme1α (IRE1α), protein kinase RNA(PKR)-like ER kinase (PERK), and activating transcription factor 6 (ATF6), which gets activated during ER stress [31]. In normal conditions, GRP78 (BiP), a chaperone, keeps these sensors in an inactive state. When unfolded or misfolded protein accumulates, GRP78 dissociates from these sensors, leading to their activation [31]. Of these, PERK is an essential UPR protein that gets activated by autophosphorylation upon ER stress. Phosphorylated PERK further phosphorylates eIF2α and inactivates general protein translation [30]. Our study revealed that F2 induces ER stress, as evident by increased phosphorylation of PERK and eIF2α, the major indicators of ER stress. Additionally, it is known that activated ATF6 translocates to the nucleus and induces the expression of chaperones, including GRP78, to aid in protein folding [31]. Indeed, we found a significant increase in the levels of GRP78 post-F2 treatment. Akt, a serine/threonine kinase, plays a

central role in cancer cell growth and survival under normal and stressful conditions [32]. Interestingly, previous reports have shown that conventional chemotherapeutic drugs, including cisplatin and doxorubicin, while inducing apoptosis, also trigger phosphorylation and activation of Akt, which further activates the survival pathway and may counteract drug-induced cell death [33, 34]. We also observed the activation of Akt in HeLa and ME-180 cells, as indicated by the increased phosphorylation of Akt after F2 treatment.

In order to gain better insight into the relation of ROS with ER stress and apoptosis in our model system, we studied the effect of NAC, a well-known antioxidant. Surprisingly, in the presence of NAC, we found even higher cell death in HeLa and ME-180 cells compared to cells treated with F2 alone. The results further demonstrated the differential effect of NAC on ROS levels in F2 treated HeLa and ME-180 cells. In HeLa cells, NAC failed to reduce the F2 induced ROS levels, whereas it decreased the ROS levels to a minimum in ME-180 cells. Additionally, we did not find any changes in ER stress upon NAC treatment, which suggests that F2 mediated ER stress is independent of ROS levels, and ROS is rather a consequence than a cause of F2 induced cell death. However, how NAC exacerbated the F2 mediated cytotoxicity was still not clear. In several studies, it has been reported that NAC can inhibit the activation of Akt in different cancer types, including cervical cancer, and can sensitize the cells to different chemotherapeutic drugs [34–36]. In accordance with these studies, our results showed that NAC significantly inhibited the F2 induced Akt activation and, subsequently, the cell survival pathway, which might render the cells more susceptible to cell death.

Experimental evidence shows that many drug candidates that exhibit high anticancer activity in monolayer culture lose efficacy in in vivo preclinical settings [37]. This can be attributed to the inability of monolayer cultures to mimic the complexity of the tumor microenvironment. Today, the use of 3D MCTS is considered to be an essential platform for drug screening as it bridges the gap between conventional monolayer testing and animal models [18, 37]. In fact, our results from APH spheroid viability assay and PI staining demonstrated that F2 exerted a dose-dependent cytotoxic effect on 3D HeLa spheroids. Moreover, we monitored the spheroids for 15 days following treatment to explore the aftereffect of F2 on spheroid growth. Interestingly, we observed slight growth in spheroids at a lower dose of 12.5 µg/mL F2. In contrast, spheroid growth was completely abrogated at higher doses of F2, which signifies the strong therapeutic potential of F2.

Studies have shown that neem limonoids, including nimbolide, azadirachtin, gedunin, azadiradione, and epoxyazadiradione, are responsible for the anticancer activity of neem extracts [8, 9, 21, 38, 39]. The phytochemical screening of F2 revealed six compounds, including five limonoids and a flavonoid, which have already been reported earlier from the same species [40, 41]. Among these six compounds, the flavonoid nicotiflorin has also been isolated from other plant species and reported for its hepatoprotective, cardioprotective, neuroprotective, and anti-inflammatory effects [40, 42]. The anticancer potential of nicotiflorin has been investigated recently against lung carcinoma [43]. However, apart from insecticidal activity, no studies were found related to the anticancer activity of the identified limonoids [41]. Hence, this is the first study to demonstrate the anticancer activity of the neem stem bark-derived limonoid-rich fraction and suggests the necessity to further investigate the identified compounds independently or in combination to enhance our knowledge to develop new therapeutic drugs.

Conclusion

In conclusion, this is the first study demonstrating the anticancer potential and mechanism of limonoid-rich fraction F2 derived from the DCM extract of *Azadirachta indica* stem bark against cervical cancer. More importantly, our study highlighted the specificity of F2 against cervical cancer cells and showed that F2 induced ROS-independent ER stress and cell death. Furthermore, F2 exerted a strong growth inhibitory effect on 3D HeLa spheroids, establishing its therapeutic efficacy against cervical cancer. The presence of limonoids and a flavonoid could explain the anticancer properties of F2. However, further studies to identify the extent of their contribution to the anticancer activity of F2 are required to utilize their full potential as anticancer agents in combating cervical cancer and possibly other cancer types.

Abbreviations

APH	Acid phosphatase assay
ATCC	American type culture collection
DCM	Dichloromethane
DMEM	Dulbecco's Modified Eagle Medium
DMSO	Dimethyl sulfoxide
ESI-MS	Electrospray ionization-mass spectrometry
FBS	Fetal bovine serum
FTIR	Fourier-transform infrared spectroscopy
^{1}H NMR	Nuclear magnetic resonance
MCTS	Multicellular tumor spheroids
MTT	3-(4,5-dimethylthiazol-2-yl)-2,5-diphenyltetrazolium bromide
NAC	N-Acetyl cysteine
ROS	Reactive oxygen species
RPMI	Roswell Park Memorial Institute
TLC	Thin-layer chromatography
UPR	Unfolded Protein Response

Supplementary Information

The online version contains supplementary material available at https://doi.org/10.1186/s12885-025-13601-6.

Supplementary Material 1.

Supplementary Material 2.

Acknowledgements
We thank the Indian Institute of Science Education and Research Kolkata for providing the necessary support. The graphical abstract was created with BioRender.com.

Authors' contributions
SK and JDS conceptualized and designed the study. SK, along with GM and SD, performed all the experiments. SK analyzed the data, prepared all the figures and wrote the original draft of the manuscript. BD and PG helped in the analytical characterization of fraction. JDS supervised the overall study, acquired funding, and reviewed the manuscript. All authors read and approved the final manuscript. All authors agree to be accountable for all aspects of work, ensuring integrity and accuracy.

Funding
This work was supported under the grant name System Medicine Cluster (SyMeC) by the Department of Biotechnology, India, research grant (BT/MEDII/NIBMG/SYMEC/2014/Vol.II). We thank the Council of Scientific and Industrial Research (CSIR) India for providing fellowship to SK. We thank IISER-Kolkata for providing fellowship to BD and GM. We thank the Department of Science and Technology for providing a fellowship to SD. The funding bodies had no role in the design of the study, collection, analysis, or interpretation of data or in writing the manuscript.

Data availability
The datasets used and/or analyzed during the current study are available from the corresponding author upon reasonable request.

Declarations

Ethics approval and consent to participate
Not applicable.

Consent for publication
Not applicable.

Competing interests
The authors declare no competing interests.

Author details
[1]Department of Biological Sciences, Indian Institute of Science Education and Research Kolkata, Mohanpur, West Bengal 741246, India. [2]Department of Chemical Sciences, Indian Institute of Science Education and Research Kolkata, Mohanpur, West Bengal 741246, India.

Received: 14 January 2024 Accepted: 28 January 2025
Published online: 25 February 2025

References

1. Bray F, Laversanne M, Sung H, Ferlay J, Siegel RL, Soerjomataram I, et al. Global cancer statistics 2022: GLOBOCAN estimates of incidence and mortality worldwide for 36 cancers in 185 countries. CA Cancer J Clin. 2024;February:229–63.
2. Aoki ES, Yin R, Li K, Bhatla N, Singhal S, Ocviyanti D, et al. National screening programs for cervical cancer in Asian countries. J Gynecol Oncol. 2020;31:1–9.
3. Singh D, Vignat J, Lorenzoni V, Eslahi M, Ginsburg O, Lauby-Secretan B, et al. Global estimates of incidence and mortality of cervical cancer in 2020: a baseline analysis of the WHO global cervical cancer elimination initiative. Lancet Glob Heal. 2023;11:e197–206. https://doi.org/10.1016/S2214-109X(22)00501-0.
4. Burmeister CA, Khan SF, Schäfer G, Mbatani N, Adams T, Moodley J, et al. Cervical cancer therapies: current challenges and future perspectives. Tumour Virus Res. 2022;13:200238.
5. Ouyang L, Luo Y, Tian M, Zhang SY, Lu R, Wang JH, et al. Plant natural products: from traditional compounds to new emerging drugs in cancer therapy. Cell Prolif. 2014;47:506–15. https://doi.org/10.1111/cpr.12143.
6. Arora N, Koul A, Bansal MP. Chemopreventive activity of Azadirachta indica on two-stage skin carcinogenesis in murine model. Phyther Res. 2011;25:408–16.
7. Gupta SC, Prasad S, Tyagi AK, Kunnumakkara AB, Aggarwal BB. Neem (Azadirachta indica): an Indian traditional panacea with modern molecular basis. Phytomedicine. 2017;34:14–20. https://doi.org/10.1016/j.phymed.2017.07.001.
8. Patel MJ, Tripathy S, Mukhopadhyay KD, Wangjam T, Cabang AB, Morris J, et al. A supercritical CO 2 extract of neem leaf (A. indica) and its bioactive liminoid, nimbolide, suppresses colon cancer in preclinical models by modulating pro-inflammatory pathways. Mol Carcinog. 2018;57:1156–65. https://doi.org/10.1002/mc.22832.
9. Kikuchi T, Ishii K, Noto T, Takahashi A, Tabata K, Suzuki T, et al. Cytotoxic and apoptosis-inducing activities of limonoids from the seeds of azadirachta indica (neem). J Nat Prod. 2011;74:866–70. https://doi.org/10.1021/np100783k.
10. Wu Q, Kohli M, Bergen HR, Cheville JC, Karnes RJ, Cao H, et al. Preclinical evaluation of the supercritical extract of azadirachta indica (neem) leaves in vitro and in vivo on inhibition of prostate cancer tumor growth. Mol Cancer Ther. 2014;13:1067–77. https://doi.org/10.1158/1535-7163.MCT-13-0699.
11. Fujiwara T, Takeda T, Ogihara Y, Shimizu M, Nomura T, Tomita Y. Studies on the structure of polysaccharides from the bark of Melia azadirachta. Chem Pharm Bull. 1982;30:4025–30.
12. Kumar S, Mulchandani V, Das Sarma J. Methanolic neem (Azadirachta indica) stem bark extract induces cell cycle arrest, apoptosis and inhibits the migration of cervical cancer cells in vitro. BMC Complement Med Ther. 2022;22:1–16. https://doi.org/10.1186/s12906-022-03718-7.
13. Reuben Kitimu S, Kirira P, Sokei J, Ochwangi D, Mwitari P, Maina N. Biogenic synthesis of silver nanoparticles using Azadirachta indica methanolic bark extract and their anti-proliferative activities against DU-145 human prostate cancer cells. Afr J Biotechnol. 2022;21:64–72. https://doi.org/10.5897/AJB2021.17424.
14. Sarkar L, Oko L, Gupta S, Bubak AN, Das B, Gupta P, et al. Azadirachta indica A. juss bark extract and its Nimbin isomers restrict β -coronaviral infection and replication bioactivity of Indian Medicinal plants. Virology. 2022;569:13–28. https://doi.org/10.1016/j.virol.2022.01.002.
15. Franken NAP, Rodermond HM, Stap J, Haveman J, van Bree C. Clonogenic assay of cells in vitro. Nat Protoc. 2006;1:2315–9.
16. Porameesanaporn Y, Uthaisang-Tanechpongtamb W, Jarintanan F, Jongrungruangchok S, Wongsatayanon BT. Terrein induces apoptosis in HeLa human cervical carcinoma cells through p53 and ERK regulation. Oncol Rep. 2013;29:1600–8.
17. Foty R. A simple hanging drop cell culture protocol for generation of 3D spheroids. J Vis Exp. 2011;20:4–7.
18. Friedrich J, Seidel C, Ebner R, Kunz-Schughart LA. Spheroid-based drug screen: considerations and practical approach. Nat Protoc. 2009;4:309–24. https://doi.org/10.1038/nprot.2008.226.
19. Ivanov DP, Parker TL, Walker DA, Alexander C, Ashford MB, Gellert PR, et al. Multiplexing spheroid volume, resazurin and acid phosphatase viability assays for high-throughput screening of tumour spheroids and stem cell neurospheres. PLoS One. 2014;9:1–14.

20. Chandele A, Prasad V, Jagtap JC, Shukla R, Shastry PR. Upregulation of survivin in G2/M cells and inhibition of caspase 9 activity enhances resistance in staurosporine-induced apoptosis. Neoplasia. 2004;6:29–40.
21. Saleem S, Muhammad G, Hussain MA, Bukhari SNA. A comprehensive review of phytochemical profile, bioactives for pharmaceuticals, and pharmacological attributes of Azadirachta indica. Phyther Res. 2018;32:1241–72. https://doi.org/10.1002/ptr.6076.
22. Hanahan D, Weinberg RA. Hallmarks of cancer: the next generation. Cell. 2011;144:646–74. https://doi.org/10.1016/j.cell.2011.02.013.
23. Brown NR, Korolchuk S, Martin MP, Stanley WA, Moukhametzianov R, Noble MEM, et al. CDK1 structures reveal conserved and unique features of the essential cell cycle CDK. Nat Commun. 2015;6:1–12.
24. Hsueh K-C, Lin C-L, Tung J-N, Yang S-F, Hsieh Y-H. Nimbolide induced apoptosis by activating ERK-mediated inhibition of c-IAP1 expression in human hepatocellular carcinoma cells. Environ Toxicol. 2018;33:913–22.
25. Hsieh Y-H, Lee C-H, Chen H-Y, Hsieh S-C, Lin C-L, Tsai J-P. Induction of cell cycle arrest, DNA damage, and apoptosis by nimbolide in human renal cell carcinoma cells. Tumor Biol. 2015;36:7539–47. https://doi.org/10.1007/s13277-015-3477-0.
26. Riahi-Chebbi I, Souid S, Othman H, Haoues M, Karoui H, Morel A, et al. The phenolic compound Kaempferol overcomes 5-fluorouracil resistance in human resistant LS174 colon cancer cells. Sci Rep. 2019;9:1–20.
27. Shahar N, Larisch S. Inhibiting the inhibitors: targeting anti-apoptotic proteins in cancer and therapy resistance. Drug Resist Updat. 2020;52:100712. https://doi.org/10.1016/j.drup.2020.100712.
28. Heo JR, Lee GA, Kim GS, Hwang KA, Choi KC. Phytochemical-induced reactive oxygen species and endoplasmic reticulum stress-mediated apoptosis and differentiation in malignant melanoma cells. Phytomedicine. 2018;39:100–10. https://doi.org/10.1016/j.phymed.2017.12.006.
29. Zhou Y, Shu F, Liang X, Chang H, Shi L, Peng X, et al. Ampelopsin induces cell growth inhibition and apoptosis in breast cancer cells through ROS generation and endoplasmic reticulum stress pathway. PLoS One. 2014;9:e89021.
30. Tabas I, Ron D. Integrating the mechanisms of apoptosis induced by endoplasmic reticulum stress. Nat Cell Biol. 2011;13:184–90.
31. Szegezdi E, Logue SE, Gorman AM, Samali A. Mediators of endoplasmic reticulum stress-induced apoptosis. EMBO Rep. 2006;7:880–5.
32. Song M, Bode AM, Dong Z, Lee MH. AKt as a therapeutic target for cancer. Cancer Res. 2019;79:1019–31.
33. Winograd-Katz SE, Levitzki A. Cisplatin induces PKB/Akt activation and p38MAPK phosphorylation of the EGF receptor. Oncogene. 2006;25:7381–90.
34. Wang H, Lu Y, Wang M, Shen A, Wu Y, Xu X, et al. Src inhibitor dasatinib sensitized gastric cancer cells to cisplatin. Med Oncol. 2023;40:1–13. https://doi.org/10.1007/s12032-022-01879-6.
35. Lee MF, Chan CY, Hung HC, Chou IT, Yee AS, Huang CY. N-acetylcysteine (NAC) inhibits cell growth by mediating the EGFR/Akt/HMG box-containing protein 1 (HBP1) signaling pathway in invasive oral cancer. Oral Oncol. 2013;49:129–35. https://doi.org/10.1016/j.oraloncology.2012.08.003.
36. Zhang T, Zhu X, Wu H, Jiang K, Zhao G, Shaukat A, et al. Targeting the ROS/PI3K/AKT/HIF-1α/HK2 axis of breast cancer cells: combined administration of polydatin and 2-Deoxy-d-glucose. J Cell Mol Med. 2019;23:3711–23.
37. Stock K, Estrada MF, Vidic S, Gjerde K, Rudisch A, Santo VE, et al. Capturing tumor complexity in vitro: comparative analysis of 2D and 3D tumor models for drug discovery. Sci Rep. 2016;6:1–15.
38. Kumar D, Haldar S, Gorain M, Kumar S, Mulani FA, Yadav AS, et al. Epoxyazadiradione suppresses breast tumor growth through mitochondrial depolarization and caspase-dependent apoptosis by targeting PI3K/Akt pathway. BMC Cancer. 2018;18:1–17.
39. Nagini S, Palrasu M, Bishayee A. Limonoids from neem (Azadirachta Indica A. Juss.) are potential anticancer drug candidates. Med Res Rev. 2023;April 2022:1–40.
40. Vergallo C, Panzarini E, Dini L. High performance liquid chromatographic profiling of antioxidant and antidiabetic flavonoids purified from Azadirachta indica (neem) leaf ethanolic extract. Pure Appl Chem. 2019;91:1631–40.
41. Simmonds MSJ, Jarvis AP, Johnson S, Jones GR, Morgan ED. Comparison of anti-feedant and insecticidal activity of nimbin and salannin photo-oxidation products with neem (Azadirachta indica) limonoids. Pest Manag Sci. 2004;60:459–64.
42. Li R, Guo M, Zhang G, Xu X, Li Q. Nicotiflorin reduces cerebral ischemic damage and upregulates endothelial nitric oxide synthase in primarily cultured rat cerebral blood vessel endothelial cells. J Ethnopharmacol. 2006;107:143–50.
43. Li Y, Yu X, Wang Y, Zheng X, Chu Q. Kaempferol-3-O-rutinoside, a flavone derived from Tetrastigma hemsleyanum, suppresses lung adenocarcinoma via the calcium signaling pathway. Food Funct. 2021;12:8351–65.

Publisher's note

Springer Nature remains neutral with regard to jurisdictional claims in published maps and institutional affiliations.